

## Article

# Intergranular Corrosion and Microstructural Evolution in a Newly Designed Al-6Mg Alloy

Kweon-Hoon Choi <sup>1,2</sup>, Bong-Hwan Kim <sup>2,\*</sup>, Da-Bin Lee <sup>2</sup>, Seung-Yoon Yang <sup>2</sup>, Nam-Seok Kim <sup>2</sup>, Seong-Ho Ha <sup>2</sup>, Young-Ok Yoon <sup>2</sup>, Hyun-Kyu Lim <sup>2</sup> and Shae-Kwang Kim <sup>2</sup>

<sup>1</sup> Department of Industrial Materials and Smart Manufacturing Engineering, Korea University of Science and Technology, Daejeon 34113, Korea; kchoi74@kitech.re.kr

<sup>2</sup> Advanced Process and Materials R&BD Group, Korea Institute of Industrial Technology (KITECH), Cheonan 31056, Korea; dabin25@kitech.re.kr (D.-B.L.); sy8357@kitech.re.kr (S.-Y.Y.); kimns@kitech.re.kr (N.-S.K.); shha@kitech.re.kr (S.-H.H.); veryoon@kitech.re.kr (Y.-O.Y.); hklim@kitech.re.kr (H.-K.L.); shae@kitech.re.kr (S.-K.K.)

\* Correspondence: bonghk75@kitech.re.kr; Tel.: +82-32-850-0440

**Abstract:** In this work, the microstructure and corrosion behavior of a novel Al-6Mg alloy were investigated. The alloy was prepared by casting from pure Al and Mg+Al<sub>2</sub>Ca master alloy. The ingots were homogenized at 420 °C for 8 h, hot-extruded and cold-rolled with 20% reduction (CR20 alloy) and 50% reduction (CR50 alloy). The CR50 alloy exhibited a higher value of intergranular misorientation due to a higher cold rolling reduction ratio. The average grain sizes were 19 ± 7 µm and 17 ± 9 µm for the CR20 and CR50 alloys, respectively. An intergranular corrosion (IGC) behavior was investigated after sensitization by a nitric acid mass-loss test (ASTM G67). The mass losses of both the CR20 and CR50 alloys were similar at early periods of sensitization, however, the CR20 alloy became more susceptible to IGC as the sensitization time increased. Grain size and β phase precipitation were two critical factors influencing the IGC behavior of this alloy system.

**Keywords:** light alloys; Al-Mg; high-strength; mechanical properties; intergranular corrosion; precipitation

**Citation:** Choi, K.-H.; Kim, B.-H.; Lee, D.-B.; Yang, S.-Y.; Kim, N.-S.; Ha, S.-H.; Yoon, Y.-O.; Lim, H.-K.; Kim, S.-K. Intergranular Corrosion and Microstructural Evolution in a Newly Designed Al-6Mg Alloy. *Materials* **2021**, *14*, 3314.

<https://doi.org/10.3390/ma14123314>

Academic Editor: Marián Palcut

Received: 11 May 2021

Accepted: 9 June 2021

Published: 15 June 2021

**Publisher's Note:** MDPI stays neutral with regard to jurisdictional claims in published maps and institutional affiliations.



**Copyright:** © 2021 by the authors. Licensee MDPI, Basel, Switzerland. This article is an open access article distributed under the terms and conditions of the Creative Commons Attribution (CC BY) license (<http://creativecommons.org/licenses/by/4.0/>).

## 1. Introduction

The 5xxx series Al-Mg alloys are widely used materials in the automotive industry due to their high strength-to-weight ratios, weldability, and good corrosion resistance [1–3]. Strength and ductility can be improved by adding solute Mg to the alloys because of the solid solution strengthening mechanism [4,5]. Nevertheless, as the amount of Mg increases, a selective oxidation prevails and causes a formation of oxide inclusions at elevated temperatures [6]. The rapid oxidation of magnesium alloys can be suppressed by additions of Ca [7]. With this background, a new alloying strategy has been developed. The strategy uses an Mg + Al<sub>2</sub>Ca master alloy instead of pure Mg during casting. The Mg + Al<sub>2</sub>Ca master alloy improves the oxidation resistance of Al-Mg alloys by forming a protective CaO/MgO mixed layer on the surface [8,9].

Previous studies have shown that anodic β-phase (β-Mg<sub>2</sub>Al<sub>3</sub>) precipitation along grain boundaries is an important factor affecting the intergranular corrosion (IGC) susceptibility of Al-Mg alloy [6–8]. The Mg segregation leads to anodic β-phase formation at 50–200 °C. The β-phase precipitation is referred to as sensitization [10–13]. The β-phase formation is usually observed at grain boundaries (GB), sub-grains, intermetallics, dislocations and other defects. Generally, the sequences of β precipitation have been reported as follows [14–16]:

Solid solution α → Guinier-Preston zones → β'' → β' → β precipitation

The  $\beta$  phases are electrochemically active compared to the Al matrix which leads to galvanic corrosion. The distribution and morphology of  $\beta$  precipitates affect the susceptibility of the alloy to IGC. To evaluate the IGC susceptibility, a nitric acid mass-loss test (NAMLT, ASTM G67) can be used to measure the corrosion rate.

In this research, the IGC susceptibility of sensitized Al-6Mg alloy with two different cold rolling conditions was studied. It is not yet clearly understood how the cold rolling process affects the corrosion behavior [17]. D’Antuono et al. observed that an increased rolling reduction increased the growth rate of  $\beta$  precipitation due to lowering nucleation temperature [18]. Additionally, an initial  $\beta$  precipitation was observed preferentially at low-angle grain boundaries rather than high-angle grain boundaries [19]. On the contrary, Wang et al. found that the maximum corrosion depth decreases with increasing cold rolling reduction ratio. They also stated that larger thickness reductions are attributable to an increased number of small-sized grains formed at the grain boundary, which can eventually break off the continuity of corrosion.

This paper aims to figure out the effect of cold rolling and sensitization treatment on the IGC susceptibility of a newly designed Al-6Mg alloy. In this study, a microstructure evolution of the alloy was analyzed by electron backscattered diffraction (EBSD). The continuity of  $\beta$ -phase precipitation at grain boundary was studied by scanning electron microscopy (SEM) and transmission electron microscopy (TEM). The effects of the cold rolling reduction ratio and sensitization heat treatment on the IGC susceptibility are discussed.

## 2. Materials and Methods

### 2.1. Sample Preparation

The ingots of Al-6Mg alloy were prepared in an electric resistance furnace by the casting of pure Al and Mg + Al<sub>2</sub>Ca master alloy. The ingots were homogenized at 420 °C into a plate with an extrusion ratio of 21.7:1. The initial extrusion thickness was 12 mm. The alloy was cold-rolled to 3 mm by using a 2-high mill rolling machine (FENN, East Berlin, CT, USA). The cold-rolled specimen was further annealed at 420 °C for 1 h in a box furnace and air-cooled. Finally, the alloy was cold-rolled with 20% reduction (CR20 alloy) and 50% reduction (CR50 alloy), respectively. The chemical composition of the Al-6Mg alloy is shown in Table 1. The chemical composition was measured by inductively coupled plasma-atomic emission spectroscopy (ICP-AES, SPECTRO).

**Table 1.** Chemical composition of Al-6Mg alloy (wt.%, measured by ICP-AES).

Alloy	Si	Fe	Cu	Mg	Mn	Ca	Al
Al-6Mg	0.05	0.07	<0.01	6.04	0.03	~0.02	Bal.

### 2.2. Intergranular Corrosion Test (NAMLT)

The specimens were sensitized at 100 °C for 0, 3, 7, 48, 144, and 207 h prior to corrosion testing. A nitric acid mass-loss test (NAMLT, ASTM G67) was used to determine the IGC susceptibility [20]. According to the standard, the test specimen was machined into blocks. The surfaces of the blocks were polished with 320 grit abrasive paper, and the specimen dimensions were measured to the nearest 0.02 mm. Before the test, the samples were etched in 5% NaOH (1 min at 80 °C). The initial mass of each specimen was measured on a digital scale. The samples were then immersed in 70% HNO<sub>3</sub> for 24 h. After the test, all specimens were carefully rinsed with water and brush with a stiff plastic brush. The final weight of the specimens was measured and used to calculate the mass-loss rate [20].

Microstructural evolutions of the alloys were investigated by optical microscopy (OM, Nikon MA200, Nikon, Tokyo, Japan), scanning electron microscopy (FE-SEM/EDSFEI Quanta200F, Hitachi, Japan), electron backscatter diffraction (EBSD, EDAX Hikari EBSD detector, Mahwah, NJ, USA), and transmission electron microscopy (TEM, JEOL JEM-2100F, Akishima, Japan). The obtained EBSD data were analyzed using the

MTEX software (open-source MATLAB toolbox) [21]. Image J software (open-source Java image program, NIH Image) was used to calculate the maximum intergranular corrosion depth and area.

### 3. Results

#### 3.1. Microstructure

Inverse pole figure (IPF) maps of newly developed Al-6Mg with two different cold rolling conditions are shown in Figure 1. The results reveal that the CR20 alloy has more equiaxed grains compared to the CR50 alloy. The CR50 alloy has a deformed microstructure due to a higher cold rolling reduction ratio. Figure 2 shows the orientation distribution functions (ODF) of the CR20 and the CR50 alloy. Typical deformation textures of the cold-rolled Al-6Mg alloys are also shown in Figure 2. As the cold rolling reduction ratio increased, more deformed textures tended to be obtained.

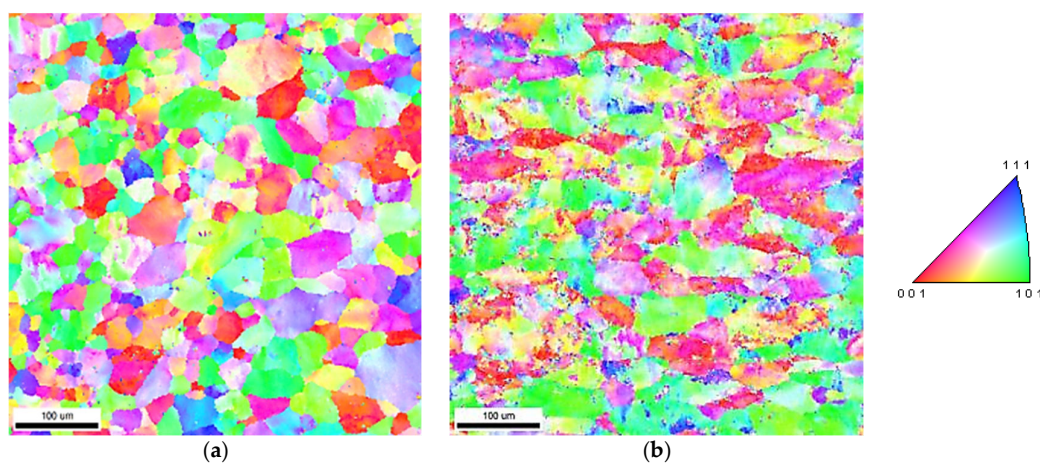


**Figure 1.** Inverse pole figure (IPF) maps of the new Al-6Mg CR20 (a) and CR50 alloys (b).

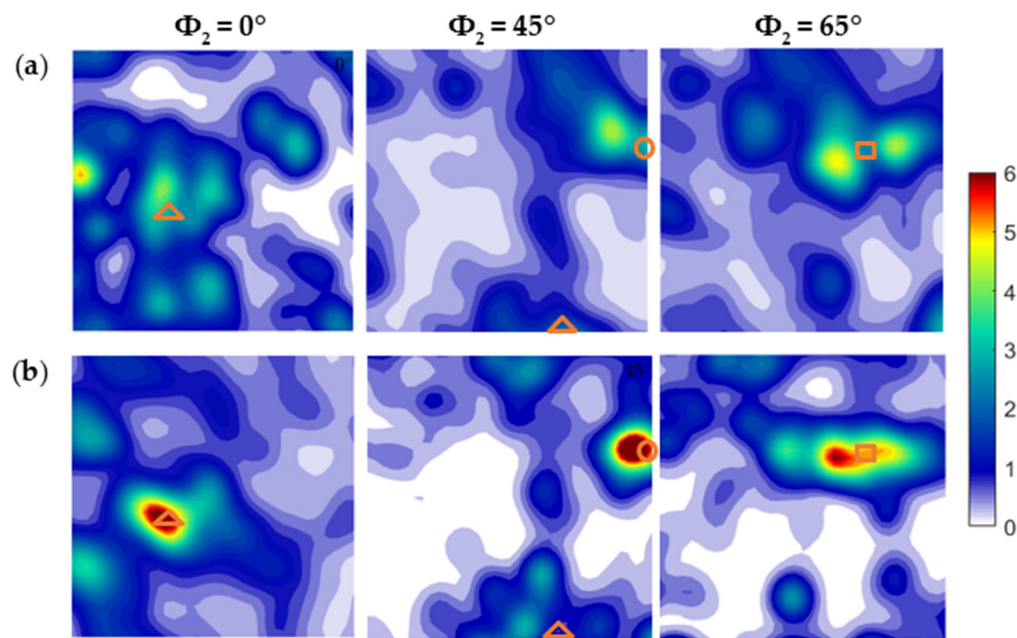


**Figure 2.** ODF sections of the new Al-6Mg CR20 (a) and CR50 alloys (b). The triangle represents Brass texture, circle is Copper texture, and the square is used for S texture.

Miller indices of the texture components for rolled samples are listed in Table 2. In the previous studies it was reported that the fraction of deformation texture components (Brass {110} <112>, Copper {112} <111> and S {123} <634>) increased while the recrystallization texture (Cube {100} <010> and Goss {011} <100>) did not change with increasing cold rolling reduction ratio in the Al-Mg alloy [22,23]. Figure 2a indicates that the CR20 alloy has an evolution of copper texture in  $\Phi_2 = 45$  section. The CR50 alloy shows a strong copper texture (Figure 2b). In addition, the CR50 alloy shows a stronger brass and S texture compared to the CR20 alloy. The results are in accordance with previous research [22,23]. However, the recrystallization texture was not found in the newly designed Al-6Mg alloy, which shows a partial disagreement with previous studies [22,23]. Therefore, the texture of the newly developed Al-6Mg alloy is yet to be completely understood.

**Table 2.** List of texture components for cold-rolled samples.

Type	Components	Orientation
Recrystallization textures	Cube	{100} <010>
	Goss	{011} <100>
Deformation textures	Brass	{011} <211>
	S	{123} <634>
	Copper	{112} <111>

Kernel average misorientation (KAM) is a measure of local grain misorientation based on the set of all neighboring misorientation. This map can be used to explain the effect of the rolling reduction ratio on the intergranular misorientation and evaluate the stored strain energy for a given point [24]. Figure 3 shows that the KAM map of the CR20 and CR50 alloys. The CR50 alloy exhibits a higher value of intergranular misorientation. As the reduction ratio of cold rolling increases, the dislocation density and volume fraction of low-angle grain boundary (LAGB) increase, which results in increasing KAM value. Figure 4 illustrates the grain size areas of CR20 and CR50 alloys. The average grain size areas of the CR20 and CR50 alloys were calculated as  $365.8 \pm 51.21 \mu\text{m}^2$  and  $283.6 \pm 87.92 \mu\text{m}^2$ , respectively. These values correspond to average grain sizes of  $19 \pm 7 \mu\text{m}$  for the CR20 alloy and  $17 \pm 9 \mu\text{m}$  for the CR50 alloy, respectively.

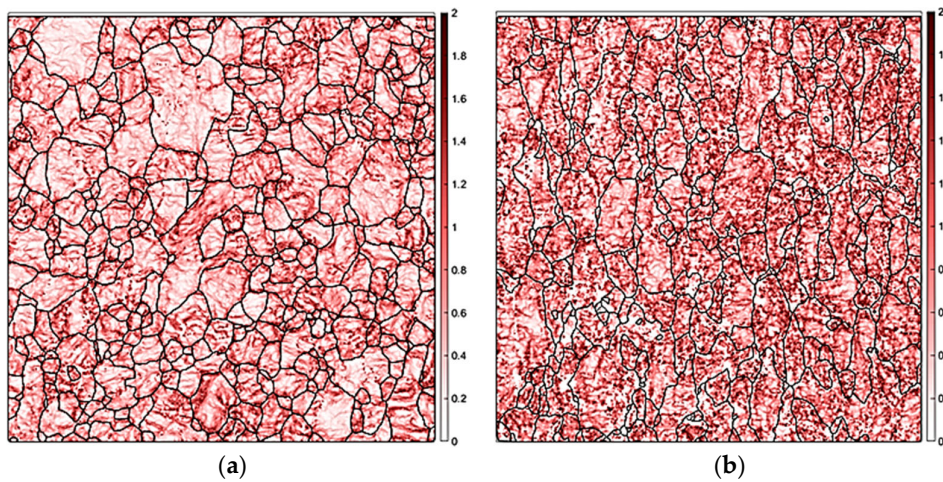


**Figure 3.** KAM maps of the CR20 (a) and CR50 alloys (b).

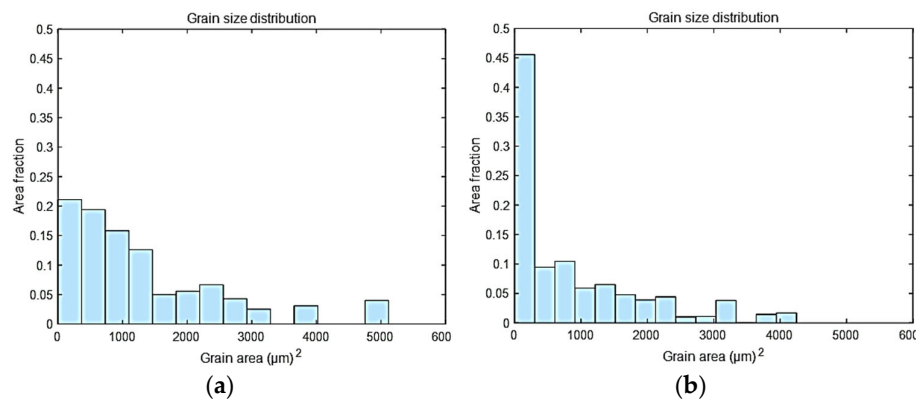


**Figure 4.** Grain size area histograms of the CR20 (a) and CR50 alloys (b).

### 3.2. Mass-Loss Test Results

Figure 5 shows the NAMLT results of the CR20 and CR50 alloys. The specimens were sensitized at 100 °C for 0, 3, 7, 48, 144, and 207 h prior to corrosion testing. The figure shows that both the CR20 and CR50 alloys had similar mass losses in concentrated nitric acid at sensitization for less than 7 h. As the sensitization time increased, the CR50 showed a slightly smaller mass-loss rate compared to the CR20 alloy. A previous study indicates that the IGC susceptibility of the Al alloys gradually decreases as the cold rolling reduction ratio increases [25].

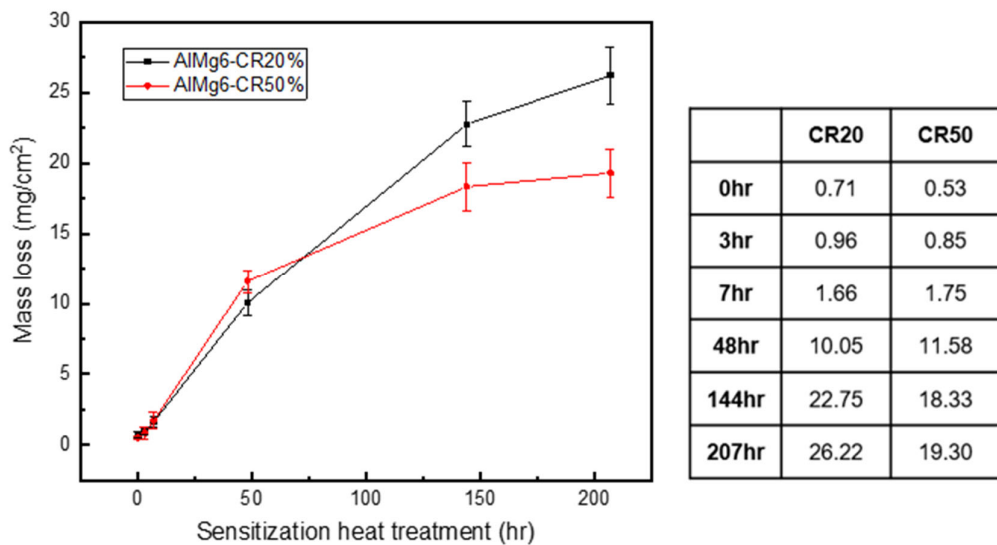


**Figure 5.** NAMLT results of the CR20 alloy and CR50 alloy with different aging times at 100 °C.

The mass-loss of 25 to 75  $\text{mg}/\text{cm}^2$  indicates that the specimen is susceptible to IGC. Smaller values correspond to better corrosion resistance. The effect of the manufacturing process on the IGC of Al-Mg alloys has been previously studied [25–27]. Zhang et al. studied how the grain size modification by various manufacturing processes affected the intergranular corrosion [26]. Previous researchers reported that the NAMLT value of AA5083 alloy (~4.5 wt% of solute Mg) was 18  $\text{mg}/\text{cm}^2$  after 8 days (192 h) of sensitization exposure at 100 °C [27]. Similar values (19  $\text{mg}/\text{cm}^2$  after 200 h of sensitization at 100 °C) were obtained in the current study. Therefore, the IGC susceptibility of high Mg-containing Al-Mg alloys appears not to be negatively affected by the cold rolling process.

### 3.3. Microstructure of Corrosion Attacked Surface

Figures 6 and 7 show the metallographic cross sections of the CR20 and CR50 alloys after the IGC test. To explore the IGC behavior, the specimens were etched using Keller's reagent for 10 s. Figures 6a and 7a indicate the estimate  $d$  corrosion depths after 0 h of sensitization. The depths are 16.75  $\mu\text{m}$  and 17.71  $\mu\text{m}$  for the CR20 and CR50 alloys, respectively. The penetration depth increases with increasing annealing time. The precipitation of  $\beta$  at grain boundaries increases with increasing sensitization time. It is assumed that the anodic precipitation of the CR50 alloy is deeper than in the CR20 alloy, which results in the IGC rate being higher in this alloy. As shown in Figures 6c and 7c, the grains start to be detached from the specimen after 48 h at 100 °C.

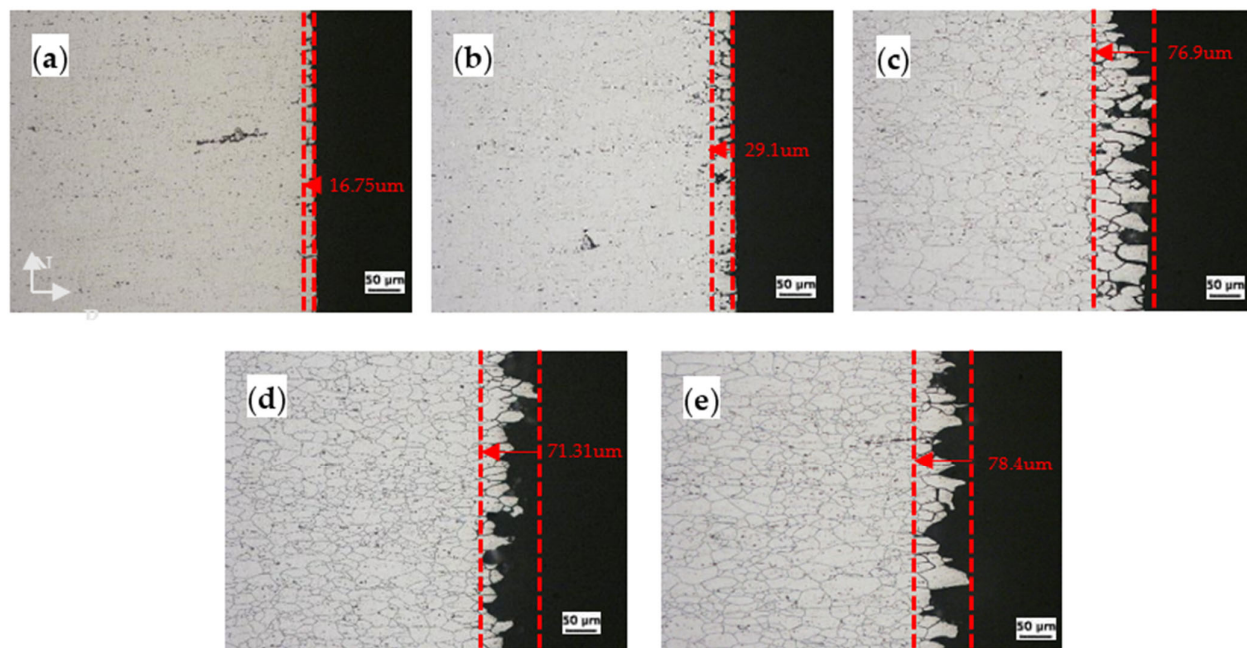


**Figure 6.** The surface of the CR20 alloy after NAMLT at different sensitization times: (a) 0 h, (b) 7 h, (c) 48 h, (d) 144 h, and (e) 207 h.

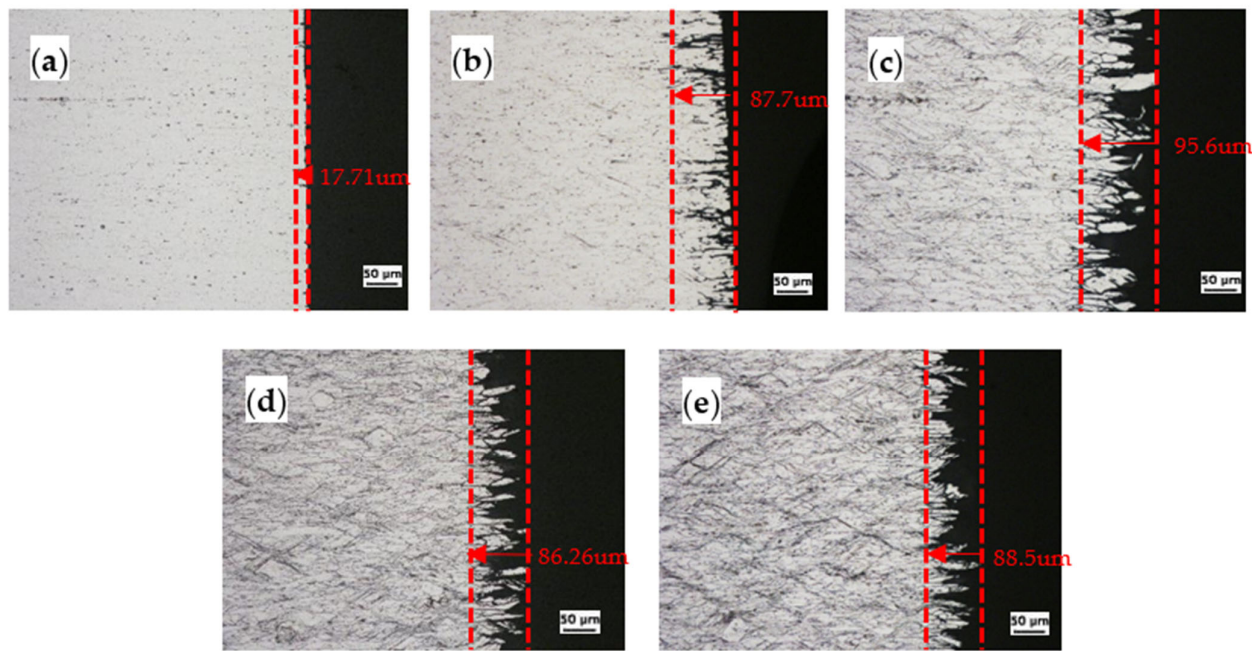


**Figure 7.** The surface of the CR50 alloy after NAMLT at different sensitization times: (a) 0 h, (b) 7 h, (c) 48 h, (d) 144 h, and (e) 207 h.

Figure 8 shows the maximum corrosion depth of both CR20 and CR50 alloys. The values are similar at the maximum sensitization time. On the other hand, the CR20 alloy shows a higher mass-loss rate compared to the CR50 alloy (Figure 5).

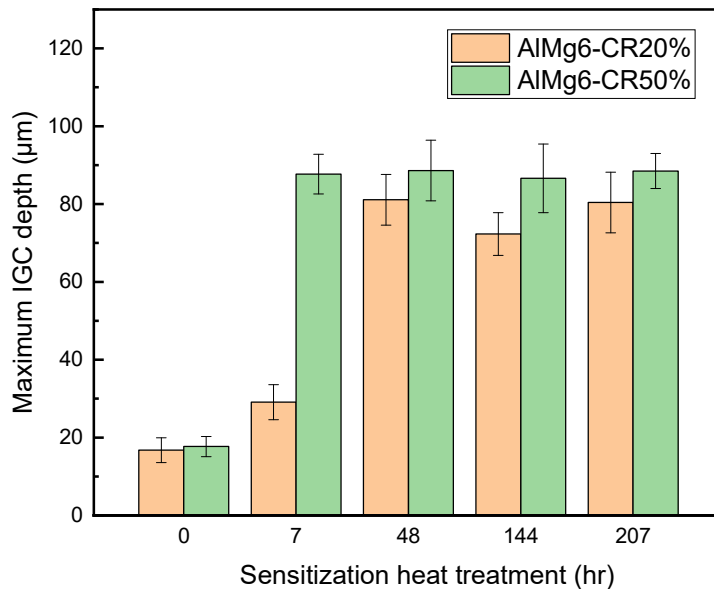


**Figure 8.** Maximum IGC depths of CR20 and CR50 alloys.

The continuity of  $\beta$  precipitation at grain boundary is critical for the IGC depth. The grain size, on the other hand, is a more important factor in the mass-loss rate at the early periods of sensitization. While there is not a significant difference between the alloys in maximum IGC depth, the NAMLT results show a higher mass-loss rate in the CR20 alloy after the long heat treatment time. This means that the CR20 alloy is more susceptible to IGC.

### 3.4. Schematic of $\beta$ Phase Distribution in Grain Boundary

Figure 9 shows the SEM images of the CR20 and CR50 alloy surface after sensitization. The grain boundary is covered with  $\beta$  precipitation. The specimens were etched using  $H_3PO_4$  etchant to selectively reveal the grain boundary covered by the anodic  $\beta$  precipitation. The continuity of  $\beta$  precipitation can be indirectly observed by the microstructure of the etched surface. At sensitization time of 7 h, the grain boundaries were more discernible in the CR50 alloy. This indicates that the CR50 alloy is more susceptible to IGC at 7 h sensitization. Figures 10 and 11 show a close look-up at the microstructure of the etched surface. The grain boundary is covered by  $\beta$  precipitation. The  $\beta$  precipitation is more discontinuous in the CR20 alloy.

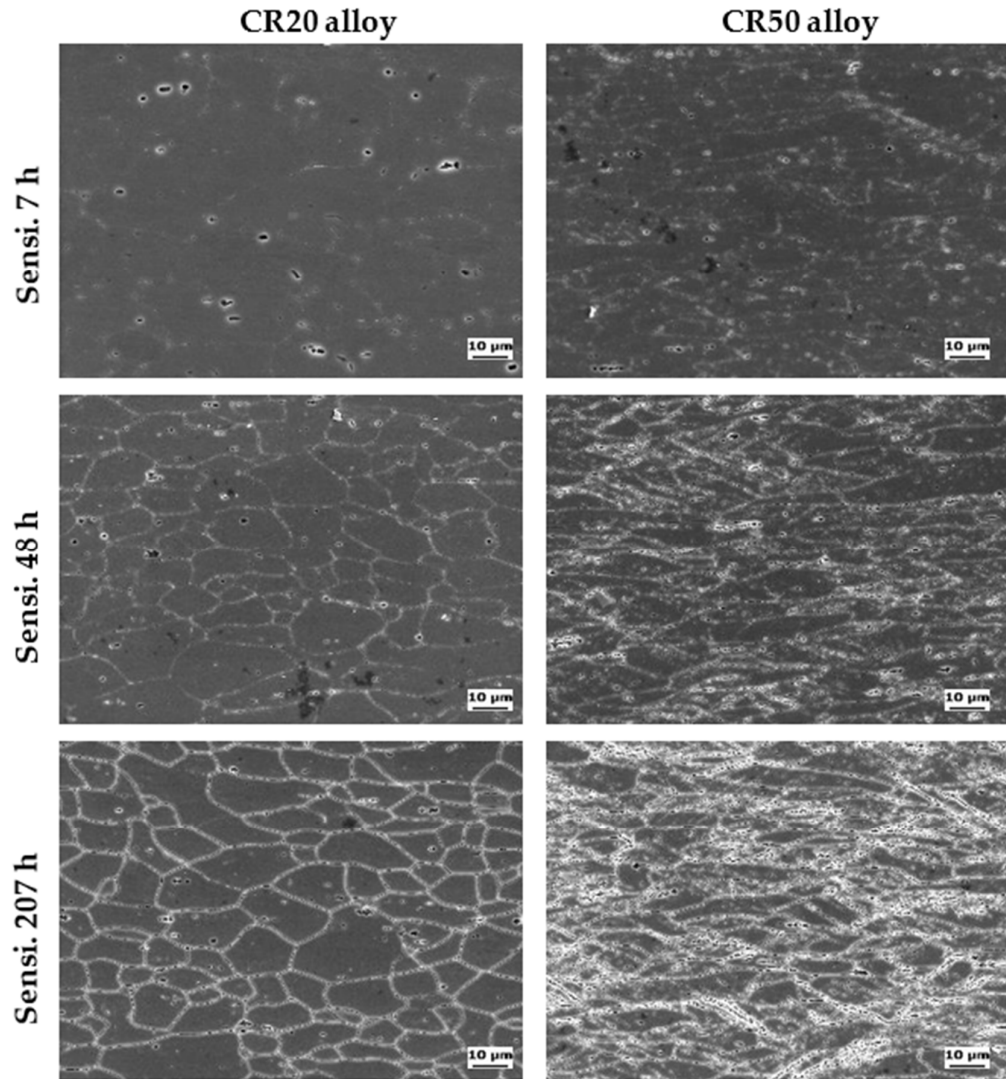


**Figure 9.** Microstructure of sensitized CR20 and CR50 alloys.

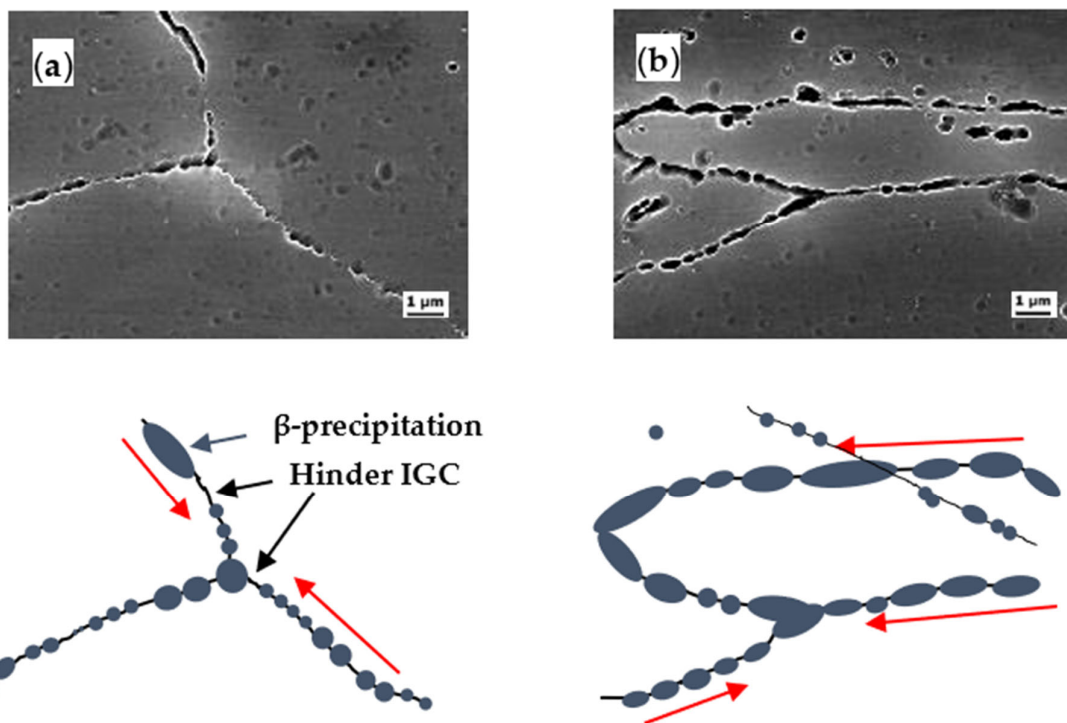


**Figure 10.** Close inspection of  $\beta$  precipitation covered grain boundary: (a) CR20 alloy, Sensi. 48 h, (b) CR50 alloy, Sensi. 48 h.

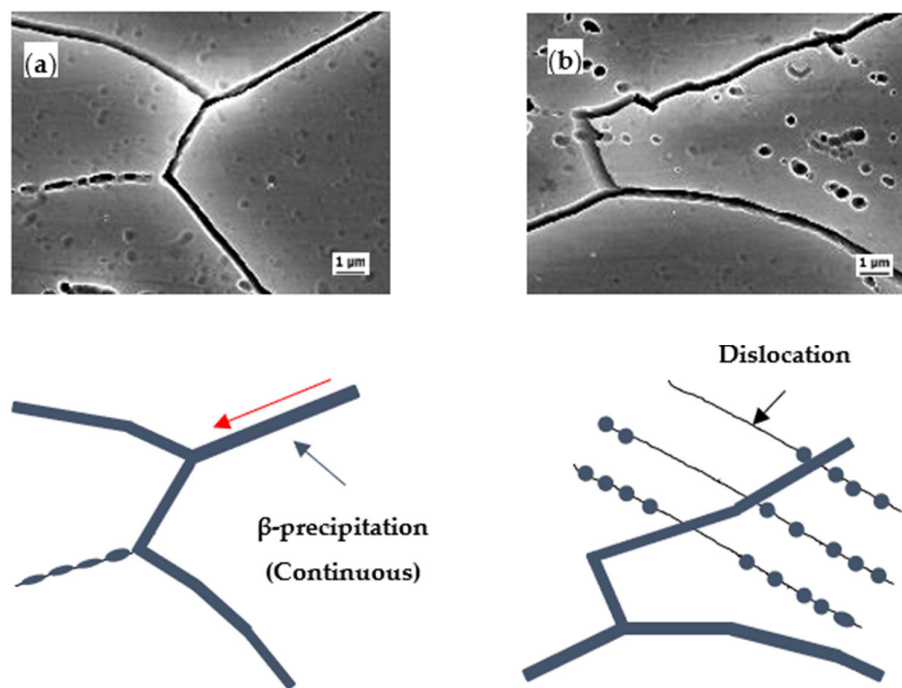


**Figure 11.** Close inspection of  $\beta$  precipitation covered grain boundary: (a) CR20 alloy, Sensi. 207 h, (b) CR50 alloy, Sensi. 207 h.

Previous studies found that the precipitate growth rates increased with rolling reduction [18,19]. A high density of dislocations can lower the activation energy, which most likely initiates the precipitation in the rolled specimen [18]. Increasing the dislocation density results in enhancing the diffusivity of Mg atoms at sensitization treatment due to pipeline diffusion [19]. On the other hand, there is no difference in the continuity of the precipitation at grain boundary at long sensitization times (Figure 11) by precipitation [18]. Considering both mass-loss results and maximum IGC depths (Figures 5 and 9), the grain size thus becomes a crucial factor in IGC at longer sensitization times.

### 3.5. Direct Observation of $\beta$ Precipitation Distribution

Figure 12 shows the thickness of the precipitates for the CR20 and CR50 alloys. The size of the precipitates was calculated from the crossline thickness of the precipitates by TEM image (Figure 13). Figure 13e represents the TEM image of the CR20 alloy with EDS mapping of magnesium at 48 h of sensitization. The thickness was found to be  $6.1 \pm 1.7$  nm for the CR20 alloy and  $7.5 \pm 3.0$  nm for the CR50 alloy at 48 h of sensitization time. The precipitate thickness at 207 h is higher. The thickness of  $\beta$ -precipitates is crucial for the IGC rate as it affects the continuity of the precipitation at the grain boundary. Figure 13a reveals that the  $\beta$  precipitation of the CR20 alloy in the early period of sensitization is discontinuous. This results in a superior corrosion resistance compared to the CR50 alloy at the early sensitization time. The size of  $\beta$  precipitates at longer sensitization times becomes larger for the CR20 alloy. Both Figure 13c,d show that  $\beta$  precipitation was almost continuously distributed at the grain boundary with almost the same thickness as shown in Figure 12. Zhang et al. also agree that the kinetics of precipitation growth is reduced with sensitization time [28]. The results of this study show that the IGC significantly depended on the grain size for long-term sensitization, as compared to the size of precipitates.

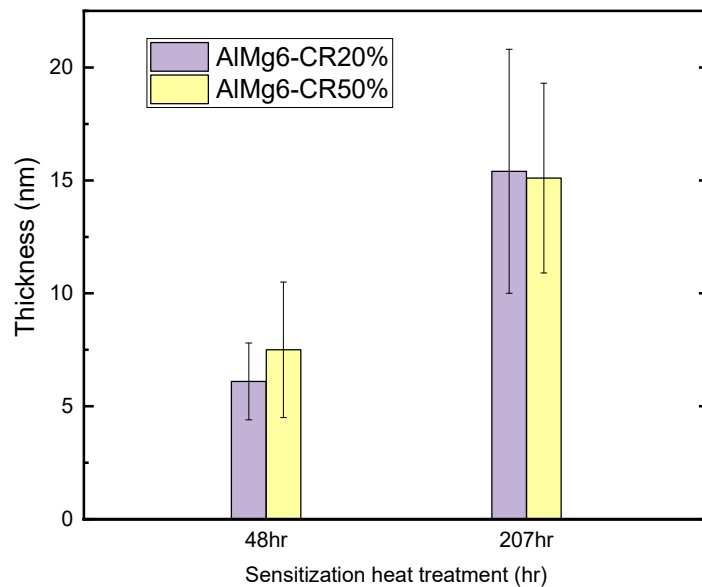


**Figure 12.** Thickness of  $\beta$ -phase precipitates in the CR20, and CR50 alloys sensitized for 48 and 207 h, respectively.

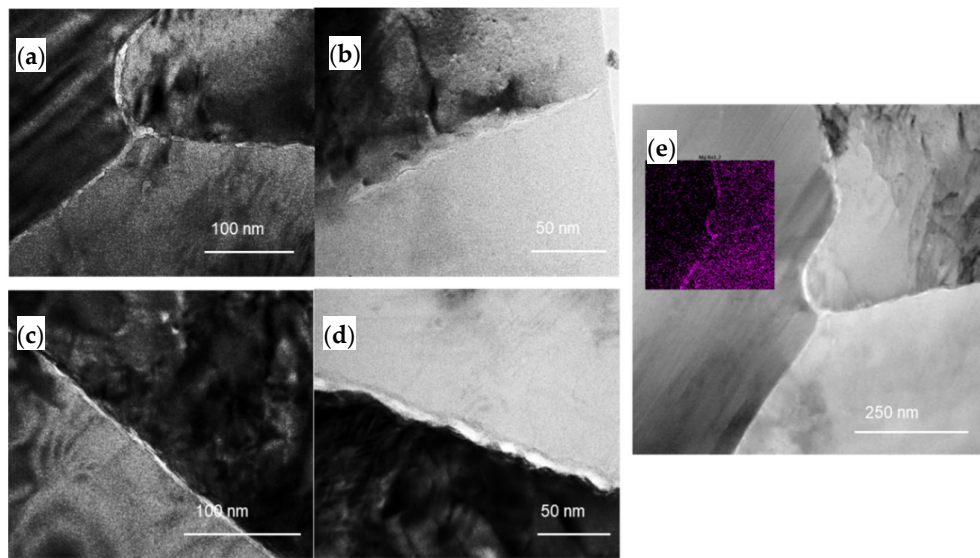


**Figure 13.** TEM of  $\beta$  precipitates in: (a) CR20 alloy, 48 h; (b) CR50 alloy, 48 h; (c) CR20 alloy, 207 h; (d) CR50 alloy, 207 h; and (e) TEM-EDS (Mg element) CR20 alloy, 48 h.

#### 4. Discussion

In this research, we found that both grain size and continuity of  $\beta$  precipitation at grain boundaries are important factors affecting the Al-Mg IGC susceptibility.

The TEM image in Figure 13 shows that the  $\beta$  precipitates are much thicker in the CR50 alloy at an early period of sensitization. The  $\beta$  precipitates thickness, however, is almost the same at long-term sensitization. Some researchers suggested that grain boundary misorientation is a crucial factor for the growth rate and the final size of  $\beta$  precipitation. These factors affect the continuity of  $\beta$  precipitation at grain boundaries [10,12,26,29–34]. Wang et al. concluded that some grain boundaries, e.g., low-angle grain boundaries generated by plastic deformation, are not susceptible to IGC [28]. On the other hand, D’Antuono reported that although the  $\beta$  precipitation was preferentially formed at low-angle grain boundary, the final size of precipitation was larger at high-angle grain boundary [18]. The influence of grain boundary plane orientation was reported to affect the continuity of precipitation. It was found that grain boundary (GB) planes close to {110} direction facilitate the  $\beta$  precipitation while the GB plane near {100} direction may be resistant to  $\beta$  precipitation [31,32].

Previous studies showed that the rolled specimen had a high resistance to IGC coming from the confluence of refined grain size and the fraction of low-angle grain boundaries [17,25,26]. In this study, it was revealed that the effect of grain size on IGC needs to be considered depending on the sensitization heat treatment which affects the formation of anodic  $\beta\text{-Mg}_2\text{Al}_3$  precipitation at the grain boundary. High dislocation density induced by cold rolling facilitates the precipitate growth rates. The formation of anodic  $\beta\text{-Mg}_2\text{Al}_3$  is affected by temperature and the presence of prior strain [35,36]. The increased dislocation density tends to lower the nucleation temperature and reduce Mg diffusion at a lower temperature [18,19]. These factors are reflected in increasing the susceptibility of the CR50 alloy in the early period of sensitization. In this situation, the dislocation density and grain boundary type affect the IGC susceptibility more significantly compared to the grain size. On the other hand, the grain size affects the IGC susceptibility of cold-rolled Al-6Mg alloy more dramatically than the grain boundary type. It was found that the large-grained material tends to be more susceptible to IGC when the precipitation is continuously formed at the grain boundary due to sufficient sensitization time.

## 5. Conclusions

This study has explored the IGC behavior of a newly designed Al-6Mg alloy with two different cold rolling conditions. It was revealed that the grain size and the continuity of  $\beta$  precipitation play an important role in IGC. The precipitation growth rate and final size of precipitates affect how the grain boundary is covered by  $\beta$  precipitation. At the early period of sensitization, the precipitation growth rate is a crucial factor in IGC. The dislocation density and grain boundary orientation affect the precipitation growth rate. The CR50 alloy has a slightly higher precipitation growth compared to the CR20 alloy because of the high density of dislocations. This results in a higher maximum IGC depth. However, the grain size effect is more dominant when the sensitization time is long enough to cover the grain boundary by anodic  $\beta$  precipitation.

**Author Contributions:** For research articles with several authors, a short paragraph specifying their individual contributions must be provided. The following statements should be used Conceptualization, K.-H.C.; methodology, K.-H.C. and H.-K.L.; software, K.-H.C.; validation, D.-B.L., S.-Y.Y. and N.-S.K.; formal analysis, S.-H.H.; investigation, D.-B.L.; resources, S.-K.K.; data curation, Y.-O.Y.; writing—original draft preparation, K.-H.C.; writing—review and editing, B.-H.K. and H.-K.L.; visualization, K.-H.C.; supervision, B.-H.K. and H.-K.L.; project administration, S.-K.K.; funding acquisition, S.-K.K. All authors have read and agreed to the published version of the manuscript.

**Funding:** This research received no external funding.

**Institutional Review Board Statement:** Not applicable.

**Informed Consent Statement:** Not applicable.

**Data Availability Statement:** Data sharing not applicable. No new data were created or analyzed in this study. Data sharing is not applicable to this article.

**Conflicts of Interest:** The authors declare no conflicts of interest.

## References

1. Polmear, I.J. *Light Alloys*, 4th ed.; Butterworth-Heinemann: Oxford, UK, 2005.
2. Sanders, R.E., Jr.; Hollinshead, P.A.; Simielli, E.A. Industrial Development of Non-Heat Treatable Aluminum Alloys. In Proceedings of the 9th International Conference on Aluminium Alloys, Brisbane, Australia, 2–5 August 2004.
3. Kubota, M.; Nie, J.F.; Muddle, B.C. Characterisation of Precipitation Hardening Response and As-Quenched Microstructures in Al-Mg-(Ag) Alloys. *Mater. Trans.* **2004**, *45*, 3256–3263, doi:10.2320/matertrans.45.3256.
4. Lee, B.-H.; Kim, S.-H.; Park, J.-H.; Kim, H.-W.; Lee, J.-C. Role of Mg in simultaneously improving the strength and ductility of Al-Mg alloys. *Mater. Sci. Eng. A* **2016**, *657*, 115–122, doi:10.1016/j.msea.2016.01.089.
5. Huskins, E.L.; Cao, B.; Ramesh, K.T. Strengthening mechanisms in an Al-Mg alloy. *Mater. Sci. Eng. A* **2010**, *527*, 1292–1298, doi:10.1016/j.msea.2009.11.056.
6. Czerwinski, F. The oxidation behaviour of an AZ91D magnesium alloy at high temperatures. *Acta Mater.* **2002**, *50*, 2639–2654, doi:10.1016/S1359-645400094-0.
7. You, B.-S.; Park, W.-W.; Chung, I.-S. The effect of calcium additions on the oxidation behavior in magnesium alloys. *Scr. Mater.* **2000**, *42*, 1089–1094.
8. Kim, B.-H.; Ha, S.-H.; Yoon, Y.-O.; Lim, H.-K.; Kim, S.K.; Kim, D.-H. Effect of Ca addition on selective oxidation of Al<sub>3</sub>Mg<sub>2</sub> phase in Al-5 mass% Mg alloy. *Mater. Lett.* **2018**, *228*, 108–111, doi:10.1016/j.matlet.2018.05.132.
9. Ha, S.-H.; Yoon, Y.-O.; Kim, B.-H.; Lim, H.-K.; Lee, T.-W.; Lim, S.-H.; Kim, S.K. Pilling-Bedworth Ratio Approach to Surface Oxidation of Al-Mg Alloys Containing Al 2 Ca and Its Experimental Verification. *Sci. Adv. Mater.* **2018**, *10*, 697–700, doi:10.1166/sam.2018.3150.
10. Steiner, M.A.; Agnew, S.R. Modeling sensitization of Al-Mg alloys via  $\beta$ -phase precipitation kinetics. *Scr. Mater.* **2015**, *102*, 55–58, doi:10.1016/j.scriptamat.2015.02.012.
11. Tan, L.; Allen, T.R. Effect of thermomechanical treatment on the corrosion of AA5083. *Corros. Sci.* **2010**, *52*, 548–554, doi:10.1016/j.corsci.2009.10.013.
12. Zhang, R.; Zhang, Y.; Yan, Y.; Thomas, S.; Davies, C.H.J.; Birbilis, N. The effect of reversion heat treatment on the degree of sensitisation for aluminium alloy AA5083. *Corros. Sci.* **2017**, *126*, 324–333, doi:10.1016/j.corsci.2017.07.015.
13. Jain, S.; Hudson, J.L.; Scully, J.R. Effects of constituent particles and sensitization on surface spreading of intergranular corrosion on a sensitized AA5083 alloy. *Electrochim. Acta* **2013**, *108*, 253–264, doi:10.1016/j.electacta.2013.06.036.
14. Jain, S.; Lim, M.L.C.; Hudson, J.L.; Scully, J.R. Spreading of intergranular corrosion on the surface of sensitized Al-4.4Mg alloys: A general finding. *Corros. Sci.* **2012**, *59*, 136–147, doi:10.1016/j.corsci.2012.02.018.

15. Yan, J.; Hodge, A.M. Study of  $\beta$  precipitation and layer structure formation in Al 5083: The role of dispersoids and grain boundaries. *J. Alloy. Compd.* **2017**, *703*, 242–250, doi:10.1016/j.jallcom.2017.01.360.
16. Lim, M.L.C.; Matthews, R.; Oja, M.; Tryon, R.; Kelly, R.G.; Scully, J.R. Model to predict intergranular corrosion propagation in three dimensions in AA5083-H131. *Mater. Des.* **2016**, *96*, 131–142, doi:10.1016/j.matdes.2016.01.089.
17. Lin, L.; Liu, Z.; Li, Y.; Han, X.; Chen, X. Effects of Severe Cold Rolling on Exfoliation Corrosion Behavior of Al-Zn-Mg-Cu-Cr Alloy. *J. Mater. Eng. Perform.* **2012**, *21*, 1070–1075, doi:10.1007/s11665-011-9978-0.
18. Scotto D’Antuono, D.; Gaies, J.; Golumbfkskie, W.; Taheri, M.L. Direct measurement of the effect of cold rolling on  $\beta$  phase precipitation kinetics in 5xxx series aluminum alloys. *Acta Mater.* **2017**, *123*, 264–271, doi:10.1016/j.actamat.2016.10.060.
19. Scotto D’Antuono, D.; Gaies, J.; Golumbfkskie, W.; Taheri, M.L. Grain boundary misorientation dependence of  $\beta$  phase precipitation in an Al-Mg alloy. *Scr. Mater.* **2014**, *76*, 81–84, doi:10.1016/j.scriptamat.2014.01.003.
20. ASTM G67-04. *Standard Test Method for Determining the Susceptibility to Intergranular Corrosion of 5XXX Series Aluminum Alloys by Mass Loss After Exposure to Nitric Acid (NAMLT Test)*; ASTM International: West Conshohocken, PA, USA, 2004.
21. Bachmann, F.; Hielscher, R.; Schaeben, H. Grain detection from 2d and 3d EBSD data—Specification of the MTEX algorithm. *Ultramicroscopy* **2011**, *111*, 1720–1733, doi:10.1016/j.ultramic.2011.08.002.
22. Duan, X.; Jiang, H.; Mi, Z.; Cheng, L.; Wang, J. Reduce the Planar Anisotropy of AA6016 Aluminum Sheets by Texture and Microstructure Control. *Crystals* **2020**, *10*, 1027, doi:10.3390/cryst10111027.
23. Choi, S.-H.; Choi, J.-K.; Kim, H.-W.; Kang, S.-B. Effect of reduction ratio on annealing texture and r-value directionality for a cold-rolled Al-5% Mg alloy. *Mater. Sci. Eng. A* **2009**, *519*, 77–87, doi:10.1016/j.msea.2009.05.063.
24. Takayama, Y.; Szpunar, J.A. Stored Energy and Taylor Factor Relation in an Al-Mg-Mn Alloy Sheet Worked by Continuous Cyclic Bending. *Mater. Trans.* **2004**, *45*, 2316–2325, doi:10.2320/matertrans.45.2316.
25. Wang, Z.; Zhu, F.; Zheng, K.; Jia, J.; Wei, Y.; Li, H.; Huang, L.; Zheng, Z. Effect of the thickness reduction on intergranular corrosion in an under-aged Al-Mg-Si-Cu alloy during cold-rolling. *Corros. Sci.* **2018**, *142*, 201–212, doi:10.1016/j.corsci.2018.07.018.
26. Zhao, Y.; Polyakov, M.N.; Mecklenburg, M.; Kassner, M.E.; Hodge, A.M. The role of grain boundary plane orientation in the  $\beta$  phase precipitation of an Al-Mg alloy. *Scr. Mater.* **2014**, *89*, 49–52, doi:10.1016/j.scriptamat.2014.07.003.
27. Zhang, R.; Knight, S.P.; Holtz, R.L.; Goswami, R.; Davies, C.H.J.; Birbilis, N. A Survey of Sensitization in 5xxx Series Aluminum Alloys. *Corrosion* **2016**, *72*, 144–159, doi:10.5006/1787.
28. Gupta, R.K.; Zhang, R.; Davies, C.H.J.; Birbilis, N. Influence of Mg Content on the Sensitization and Corrosion of Al-xMg(-Mn) Alloys. *Corrosion* **2013**, *69*, 1081–1087, doi:10.5006/0948.
29. Zhang, R.; Qiu, Y.; Qi, Y.; Birbilis, N. A closer inspection of a grain boundary immune to intergranular corrosion in a sensitised Al-Mg alloy. *Corros. Sci.* **2018**, *133*, 1–5, doi:10.1016/j.corsci.2018.01.009.
30. Ding, Q.; Zhang, D.; Zuo, J.; Hou, S.; Zhuang, L.; Zhang, J. The effect of grain boundary character evolution on the intergranular corrosion behavior of advanced Al-Mg-3wt%Zn alloy with Mg variation. *Mater. Charact.* **2018**, *146*, 47–54, doi:10.1016/j.matchar.2018.09.044.
31. Guo, C.; Zhang, H.; Wu, Z.; Wang, D.; Li, B.; Cui, J. Effects of Ag on the age hardening response and intergranular corrosion resistance of Al-Mg alloys. *Mater. Charact.* **2019**, *147*, 84–92, doi:10.1016/j.matchar.2018.10.025.
32. Ramachandran, D.C.; Murugan, S.P.; Kim, Y.-M.; Kim, D.; Kim, G.-G.; Nam, D.-G.; Jeong, C.; Do Park, Y. Effect of Microstructural Constituents on Fusion Zone Corrosion Properties of GMA Welded AA 5083 with Novel Al-Mg Welding Wires of High Mg Contents. *Met. Mater. Int.* **2020**, *26*, 1341–1353, doi:10.1007/s12540-019-00434-9.
33. Yan, J.; Heckman, N.M.; Velasco, L.; Hodge, A.M. Improve sensitization and corrosion resistance of an Al-Mg alloy by optimization of grain boundaries. *Sci. Rep.* **2016**, *6*, 26870, doi:10.1038/srep26870.
34. Holroyd NJ, H.; Burnett, T.L.; Seifi, M.; Lewandowski, J.J. Improved understanding of environment-induced cracking (EIC) of sensitized 5XXX series aluminium alloys. *Mater. Sci. Eng. A* **2017**, *682*, 613–621, doi:10.1016/j.msea.2016.11.088.
35. Nebtp, S.; Hamanai, D.; Cizeron, G. Calorimetric study of pre-precipitation and precipitation in Al-Mg alloy. *Acta Metall. Mater.* **1994**, *43*, 3583–3588.
36. Starink, M.J.; Zahra, A.-M.  $\beta'$  and  $\beta$  precipitation in an Al-Mg alloy studied by DSC and TEM. *Acta Mater.* **1998**, *46*, 3381–3397, doi:10.1016/S1359-645400053-6.